Supplementary Information

Molten salt infiltration-oxidation synergistic controlled lithium extraction from spent lithium iron phosphate batteries: an efficient, acid free, and closed-loop strategy

Jiafeng Zhang[1], Jingtian Zou[1], Di He[2*], Wenyang Hu[1], Dezhao Peng[1], Yong Li[2], Zaowen Zhao[3], Shubin Wang[4], Pengfei Li[5], Shilin Su[5], Keyi Ma[2,] Xiaowei Wang[1*]

1 National Engineering Laboratory for High-Efficiency Recovery of Refractory Nonferrous Metals, School of Metallurgy and Environment, Central South University, Changsha 410083, PR China
2 Key Laboratory for City Cluster Environmental Safety and Green Development of the Ministry of Education, School of Ecology, Environment and Resources, Guangdong University of Technology, Guangzhou, 510006, PR China
3 Special Glass Key Lab of Hainan Province, School of Materials Science and Engineering, Hainan University, Haikou 570228, China
4 State Environmental Protection Key Laboratory of Environmental Pollution Health Risk Assessment, South China Institute of Environmental Sciences, Ministry of Ecology and Environment (MEE), Guangzhou, China, 510655
5 Anhui Winking New Material Technology Co., LTD, Fuyang 236000, PR China

Email: yjywxw@csu.edu.cn
di.he@gdut.edu.cn

Supporting information: 4 tables, 11 figure

Figure S1. Flow chart of the recovery of spent $LiFePO_4$ batteries in this work

The ideal strategy is to recover S-LFP into FPO and a soluble lithium salt through a pyrogenic process, which can maximize the advantages of the process, product, and environmental protection. To further verify the feasibility of selective lithium extraction, Density flooding theory (DFT) calculations were conducted to check the feasibility of this strategy. The structural configurations of LFP and FPO were obtained from the structure database, and structural optimization calculations were performed. From the particle density of states of LFP **(Fig. S2a**), it is clear that the interaction between Li and O is weaker in LFP than that between Fe and O, thus making Li easier to be extracted. Also, **Fig. S2b** shows that the integration regions of the Fermi energy level electronic states of LFP and FPO are close, indicating the feasibility of phase transformation. The main principle of this reaction lies in the extraction of Li from LFP by forming soluble sulfates without extra byproducts. The optimized structures of FeO_6 and PO_4 are shown schematically in **Fig. S3**. Therefore, it is feasible to separate Li^+ from the olivine structure of LFP.

To further verify the types and trends of lithium salts generated by oxidation reaction from LFP, the formation advantage interval of possible lithium salts in a standard Li-S-O system was studied by thermodynamic calculation (**Table. S2-4**). The introduction of S lies in cost and corrosion grounds. As shown in **Fig. S4a**, the dominant area of Li_2O increases with the temperature increase, suggesting that it tends to form at high temperatures. In contrast, the chief area of FPO in the Fe-P-O system demonstrated the opposite trend, decreasing with the rise in temperature (**Fig. S4b**). The opposite direction indicates the non-coexistence of Li_2O and FPO. To address this issue, we try to introduce intermediates to achieve directional preparation of soluble lithium salts and found the stability trend of Li_2SO_4 is consistent with FPO, indicating the possible reaction between LFP and sulfates.

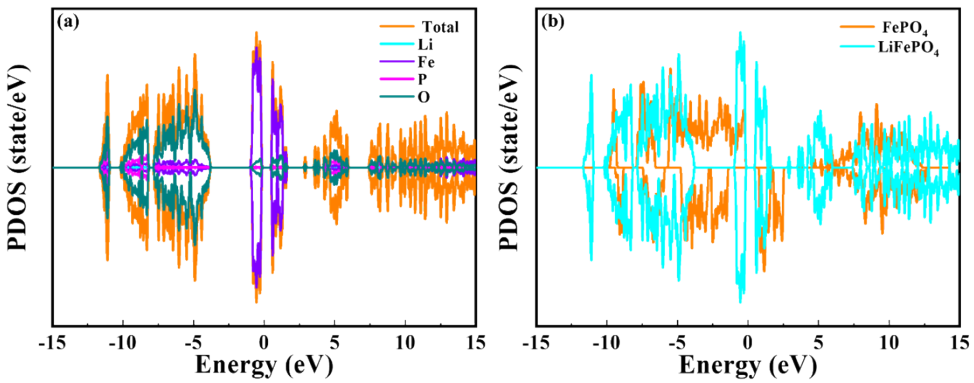

Figure S2. (a) Partial density of state of different elements in $LiFePO_4$; (b) total density of states of $LiFePO_4$ and $FePO_4$

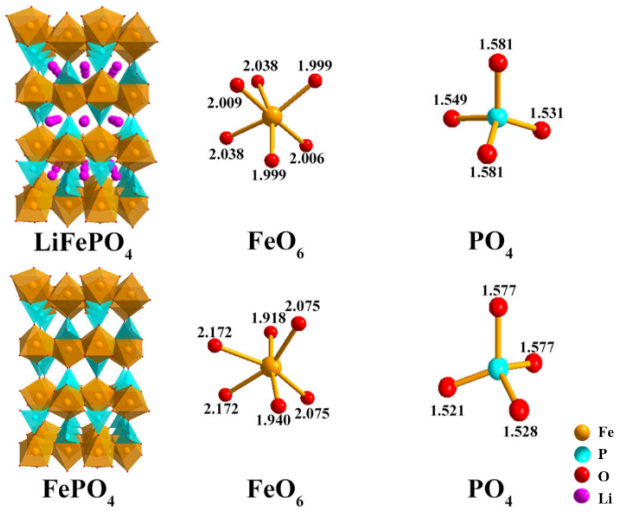

Figure S3. The optimized structures of $LiFePO_4$, $FePO_4$, FeO_6, and PO_4

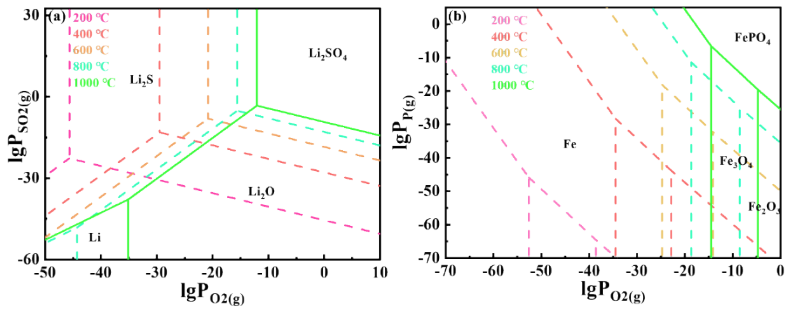

Figure S4. Thermodynamic calculation of related products of (a) Li and (b) Fe

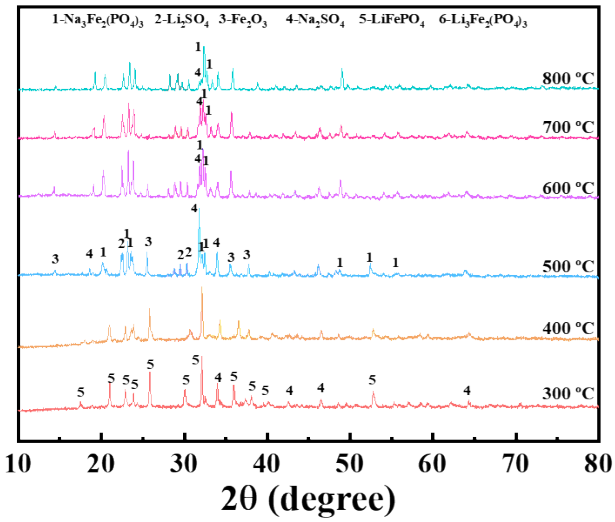

Figure S5. XRD patterns of the residues after roasting under different temperatures (300-800 °C)

$$6LiFePO_4 + 3Na_2SO_4 + O_2 = 2Na_3Fe_2(PO_4)_3 + 3Li_2SO_4 + Fe_2O_3 \qquad \text{(Equation S1)}$$

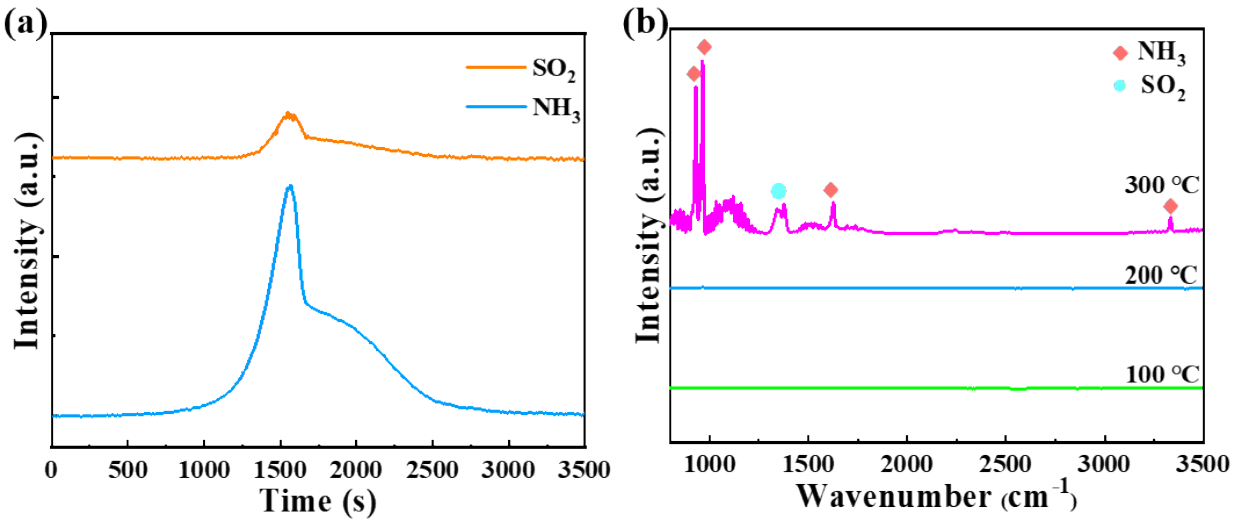

Figure S6. (a) Mass spectroscopy of the gases released during the roasting reaction; (b) mass spectroscopy of the gases released by roasting at different temperatures

The peaks in the XRD patterns for raw materials (S-LFP), leached residue (FPO), and precipitated lithium salts (Li_2CO_3) only matched the corresponding phases (**Fig. S7**). **Fig. S8** shows the XRD patterns of residues roasted under SO_2 and NH_3 atmospheres at 300 °C. The structure of S-LFP did not change after roasting, indicating that the NH_3 and SO_2 atmospheres did not contribute to the reaction.

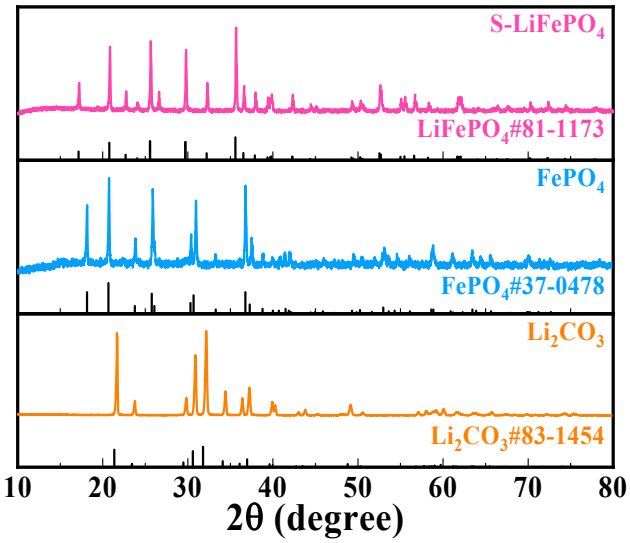

Figure S7. XRD patterns of the S-LFP, FPO, and Li_2CO_3 product

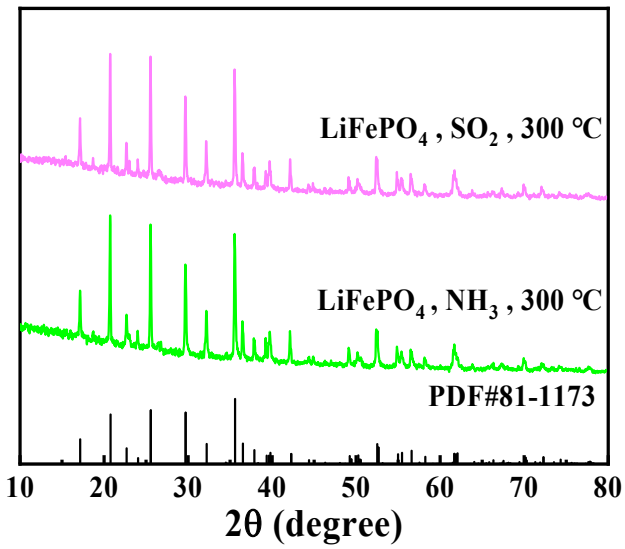

Figure S8. XRD patterns of $LiFePO_4$ after roasting in SO_2 and NH_3 atmospheres at 300 °C

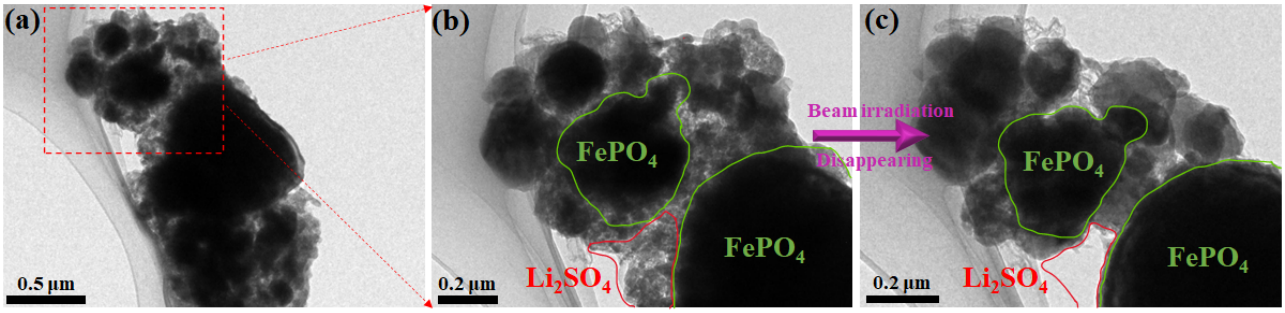

Figure S9. (a) TEM image of the particle; TEM images of roasted residue before (b) and after (c) electron beam scouring

The leaching rates of elements under different experimental conditions were studied to optimize the reaction conditions. As shown in **Figure S10a**, the temperature significantly affected the leaching rate of Li. The leaching rate of Li reached its highest point, 99.33%, at 300 °C. The leaching rate of Li decreased as the temperature was increased (above 300 °C). However, the Fe and P leaching rates remained close to 0 (**Figure S10b**). It can be seen from the leaching efficiency that 300 °C was the optimal experimental temperature (**Figure S10c**), in agreement with the previous thermodynamic calculations, and the release rate of Li^+ was maximized. **Figure S10d** shows that the leaching rate of Li reached equilibrium after 60 min, which indicated that almost all lithium was removed within approximately 60 min. In considering the leaching rates of Fe and P (**Figure S10e**) and the leaching efficiency of Li (**Figure S10f**), 60 min was chosen as the optimal experimental time.

The mixing ratios of materials also had an essential effect on the reaction. The leaching rate of Li was 99.58%. When the ratio of LFP to $(NH_4)_2SO_4$ was 1:1, the rate of Li leaching was significantly affected as the ratio was increased further. The leaching rate of Li decreased with increases in the ratio. At the same time, the efficiencies of Fe and P leaching were close to zero and remained relatively stable. **Figure S10g** shows the recovery ratio for Li, Fe, and P. The leaching rate of Li was 99.33% when the ratio was 2:1 (**Figure S10h**), and 2:1 was selected as the optimal ratio for efficient leaching of Li (**Figure S10i**) after careful consideration of economic factors. Apparently, this strategy can selectively separate lithium under the optimal conditions, and the efficiency for extraction of Li reached 99.33%. In comparison, the efficiency for extraction of Fe was 0.25%, and that for extraction of P was only 0.05%. The difference in extraction efficiencies between elements allowed effective separation to achieve a high Li extraction rate and produce high-purity FPO.

To maximize the economic value of the recovery process, the recovered FPO and Li_2CO_3 were reconverted into $LiFePO_4$ (R-LFP). The surface chemical states of Li, Fe, P, and O in S-LFP, FPO, and R-LFP were investigated with XPS analyses. As shown by the survey spectra in **Figure S11a**, the main components were Li, Fe, P, O, F, and C, consistent with the reaction system. To further verify

the changes in elemental oxidation states and bond energies during the reaction, high-resolution Fe 2p and O 1s XPS spectra were obtained (**Figure S11b** and **c**). The Fe 2p spectrum of S-LFP involves two characteristic peaks at 711.5 eV and 725.8 eV for the Fe $2p_{3/2}$ and Fe $2p_{1/2}$ states, respectively[16]. In detail, the Fe $2p_{3/2}$ peak and Fe $2p_{1/2}$ peaks can be deconvoluted into two peaks, correspond to the oxidation states Fe^{2+} (709.2 eV and 722.7 eV) and Fe^{3+} (711.3 eV and 725.5 eV), respectively[16, 29]. The binding energies of the two characteristic peaks (Fe $2p_{3/2}$ peak and Fe $2p_{1/2}$ peaks) for FPO were 712.38 eV and 726.2 eV, respectively[30, 31]. After regeneration, R-LFP also exhibited two characteristic peaks at 710.5 eV and 723.8 eV, which can be deconvoluted into Fe^{2+} peak and Fe^{3+} peak, consistent with the XPS spectra of S-LFP sample.

The Fe^{3+} oxidation state on the S-LFP surface might be due to the actual lithium deficiency and oxidation reaction[29]. As shown in **Figure S11b**, compared with S-LFP, the strength of Fe^{2+} peak for R-LFP was increased significantly, and the area ratio for Fe^{3+} was decreased correspondingly, indicating that the actual lithium deficiency and oxidation of the material were repaired after regeneration. It is worth noting that the XPS results of FPO clearly show that the peak for Fe^{2+} was almost unobserved and largely obscured by the Fe^{3+} peak, indicating Fe^{2+} was utterly converted to Fe^{3+}, proving that S-LFP was converted into FPO after the molten sulfate-regulated oxidation roasting. Besides, the O 1s spectrum was deconvoluted into two peaks corresponding to two different kinds of bonds: the strong peak at 531.8 eV was related to P-O, and the weak peak at 533.5 eV can be ascribed to Fe-O moieties on the surface (**Figure S11c**).

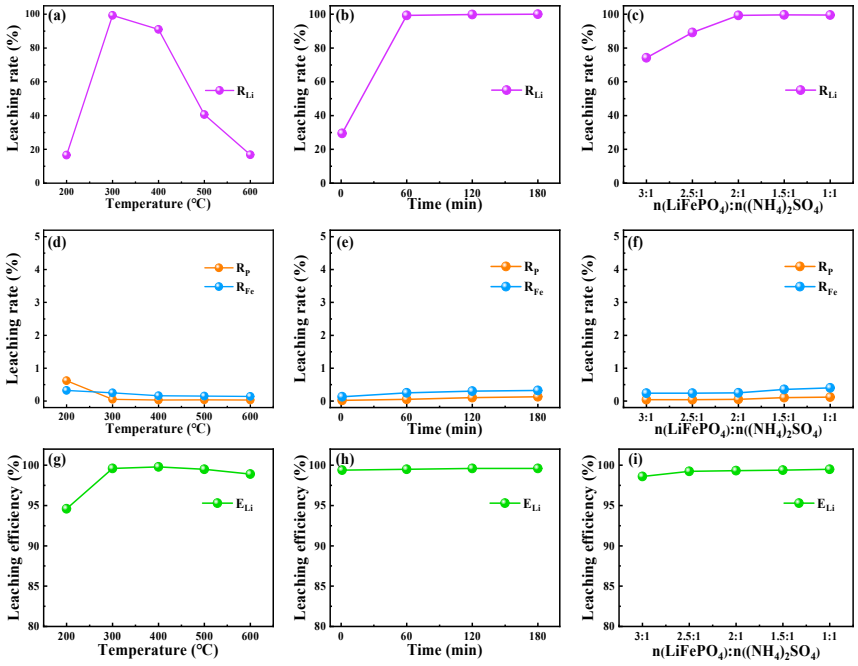

Figure S10. Effect of (a) temperature, (b) reaction time, and (c) $n(LiFePO_4)/n((NH_4)_2SO_4)$ ratio on the leaching rate of Li; effects of (d) temperature, (e) reaction time, and (f) $n(LiFePO_4)/n((NH_4)_2SO_4)$ on the leaching rates of Fe and P; effects of (g) temperature, (h) reaction time, and (i) $n(LiFePO_4)/n((NH_4)_2SO_4)$ on the leaching efficiency of Li

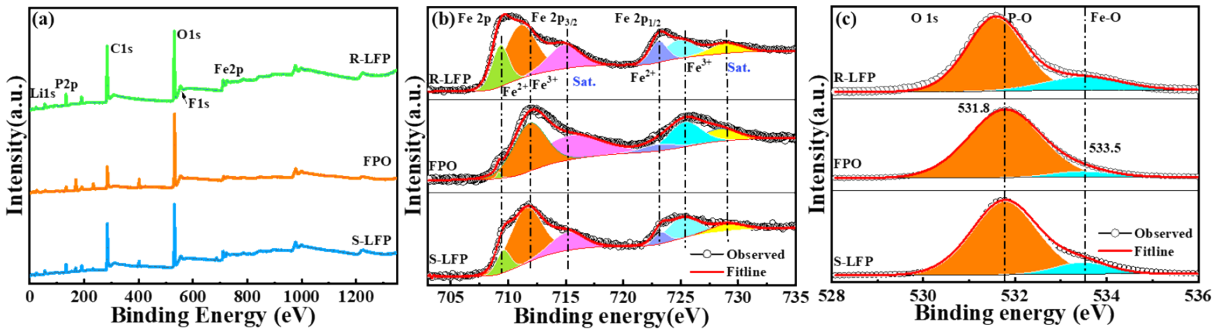

Figure S11. XPS spectra of S-LFP, FPO, and R-LFP. (a) Survey spectra; (b) high-resolution Fe 2p spectra; (c) high-resolution O1s spectra

Table S1. Main element contents of the spent $LiFePO_4$ cathode electrodes

Element	Fe	Al	Li	P	C
Wt. (%)	29	11.3	3.9	16.1	7.7

Table S2. Main element contents of the S-LFP

Element	Fe	Al	Li	P	C
Wt. (%)	35.44	<0.1	4.15	19.62	3.77

Table S3. The contents of the $FePO_4$

Element	Li	Fe	P	Al	C
Wt. (%)	<0.1	35.0	19.4	<0.1	3.81

Table S4. The contents of the Li_2CO_3

Element	Li	Fe	P	Al	Na
Wt. (%)	18.78	<0.1	<0.1	<0.1	0.12

Table S5. The Gibbs free energy for the possible products in Li-S-O system

	Composition	$\Delta_f \mathbf{G}_\mathbf{m}^\theta (kcal/mol)$
1	Li_2O	-134.117
2	Li_2S	-103.387
3	Li_2SO_4	-315.772
4	Fe_3O_4	-241.956
5	Fe_2O_3	-177.114
6	Fe_3O_4	-241.956
7	$FePO_4$	-282.559
8	SO_2	-71.724

Table S6. The possible equations involved in Li-S-O systems

	Reaction equation	Derivation of formula for Li-S-O system
1	$4Li_{(l)} + O_{2(g)} = 2Li_2O_{(s)}$	$lgP_{O2} = (lgP^{\theta} - lgK_{p1})$
2	$2Li_{(l)} + SO_{2(g)} = Li_2S_{(s)} + O_{2(g)}$	$lgP_{SO2} = lgP_{O2} + (-lgK_{p2})$
3	$2Li_{(l)} + SO_{2(g)} + O_{2(g)} = Li_2SO_{4(s)}$	$lgP_{SO2} = 2lgP^{\theta} + (-lgK_{SO2}) + (-lgK_{p3})$
4	$Li_2O_{(s)} + SO_{2(g)} = 1.5O_{2(g)} + Li_2S_{(s)}$	$lgP_{SO2} = 1.5\ lgP_{O2} + (-0.5lgP^{\theta}) + (-lgK_{p4})$
5	$Li_2O_{(s)} + SO_{2(g)} + 0.5O_{2(g)} = Li_2SO_{4(s)}$	$lgP_{SO2} = -0.5\ lgP_{O2} + (1.5\ lgP^{\theta} - lgK_{p5})$
6	$Li_2S_{(s)} + 2O_{2(g)} = Li_2SO_{4(s)}$	$lgP_{O2} = lgP^{\theta} + (-0.5lgK_{p6})$

Table S7. The possible equations involved in the Fe-P-O system

	Reaction equation	Formula derivation of Fe-P-O system
1	$4Fe + 3O_{2(g)} = 2Fe_2O_{3(s)}$	$lgP_{O2} = lgP^{\theta} + (-0.333lgK_{p17})$
2	$3Fe + 2O_{2(g)} = Fe_3O_{4(s)}$	$lgP_{O2} = lgP^{\theta} + (-0.5lgK_{p18})$
3	$Fe_{(s)} + O_{2(g)} + P_{(g)} = FePO_{4(s)}$	$lgP_P = 2lgP^{\theta} + (-lgP_{O2}) + (-lgK_{p19})$
4	$6Fe_2O_{3(s)} = O_{2(g)} + 4Fe_3O_{4(s)}$	$lgP_{O2} = lgP^{\theta} + lgK_{p20}$
5	$2Fe_2O_{3(s)} + 5O_{2(g)} + 4P_{(g)} = 4FePO_{4(s)}$	$lgP_P = 2.25lgP^{\theta} + (-1.25lgP_{O2}) + (-0.25lgK_{p21})$
6	$Fe_3O_{4(s)} + 4O_{2(g)} + 3P_{(g)} = 3FePO_{4(s)}$	$lgP_P = 2.333lgP^{\theta} + (-1.333lgP_{O2}) + (-0.333lgK_{p22})$

Table S8. DFT-calculated lattice parameters for $LiFePO_4$, $FePO_4$, and $(NH_4)_2SO_4$

Unit cell	Crystal structure	Lattice constants
$LiFePO_4$	orthorhombic	a=10.336 Å b=6.006 Å c=4.693 Å
$FePO_4$	orthorhombic	a=9.766 Å b=5.824 Å c=4.777 Å
$(NH_4)_2SO_4$	triclinic	a=5.816 Å b=7.812 Å c=10.332 Å
Li_2SO_4	monoclinic	a=4.893 Å b=7.982 Å c=8.266 Å α=71.9°

Table S9. A detailed list of economic analyses

			Hydrometallurgy Process		This work	
	Products	**Price ($ kg^{-1})**	**Mass (kg)**	**Benefits ($)**	**Mass (kg)**	**Benefits ($)**
Product	$LiFePO_4$	25.17	/	/	0.2761	6.95
	Li_2CO_3	62.39	0.0625	3.90	/	/
	Reagents	**Price ($ kg^{-1})**	**Mass (kg)**	**Cost ($)**	**Mass (kg)**	**Cost ($)**
Reagent	Na_2CO_3	0.28	0.0988	0.03	/	/
	$(NH_4)_2SO_4$	0.43	/	/	0.1155	0.05
	$C_6H_{12}O_6$	0.46	/	/	0.0264	0.012
	NaOH	0.91	0.774	0.705	/	/
	Process	**Price ($ m^{-3})**	**Consumption (m^3)**	**Cost ($)**	**Consumption (m^3)**	**Cost ($)**
Water	Acid leaching	0.372	0.12	0.046	/	/
	Water leaching	0.365	/	/	0.049	0.018
	Process	**Price ($ kW^{-1} h^{-1})**	**Consumption (kW h)**	**Cost ($)**	**Consumption (kW h)**	**Cost ($)**
Electricity	Heat treatment	0.125	2.08	0.26	2.08	0.26
	Roasting		3.76	0.47	2.64	0.33
	Leaching		0.24	0.030	0.096	0.012
	Filtration		1.00	0.125	1.00	0.125

* The price of chemical reagents comes from http://www.100ppi.com/, and the price of water and electricity comes from the commercial electricity supply in Changsha, China.

Regarding the comparative hydrometallurgical process, I would like to provide some further details. The process has been redesigned based on the conventional acid leaching process, and the specific flow of this process is illustrated in **Figure S12**. Initially, the waste $LiFePO_4$ batteries are discharged and disassembled, resulting in the recovery of cathode electrode sheets. These sheets undergo a heat treatment process to obtain the waste $LiFePO_4$ powder.

Subsequently, the waste $LiFePO_4$ powder is dissolved in a H_2SO_4 solution, resulting in the formation of aqueous solutions containing lithium, iron, and phosphorus ions. To precipitate the yellow $FePO_4$ solid from the solution, ammonia is added and the pH of the aqueous solution is adjusted to approximately 1.7. This process allows for the separation of the $FePO_4$ solid slag and the lithium-containing solutions through filtration. Furthermore, by adding a hot solution of Na_2CO_3 to the lithium-containing solution, a white solid precipitates, ultimately leading to the formation of Li_2CO_3.

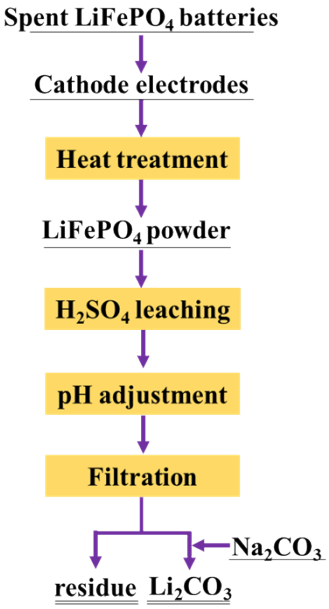

Figure S12. The process flow of comparative hydrometallurgical process.

It is important to note that in the comparative hydrometallurgical process, the resulting $FePO_4$ is not directly inherited from the original waste $LiFePO_4$ particles. Instead, it is obtained by rapidly adjusting the pH of the solution. However, the resulting $FePO_4$ particles are relatively small in size, as depicted in **Figure S13**, and cannot be utilized directly as precursors for the synthesis of lithium iron phosphate materials. Therefore, in this study, we did not focus on treating the $FePO_4$ solid slag.

For the pricing information of chemical reagents, we have sourced the data from http://www.100ppi.com/. As for the cost of water and electricity, we have obtained this information from the commercial electricity supply in Changsha, China. We have included a relevant description in the supporting materials to provide transparency regarding our sources and methodology.

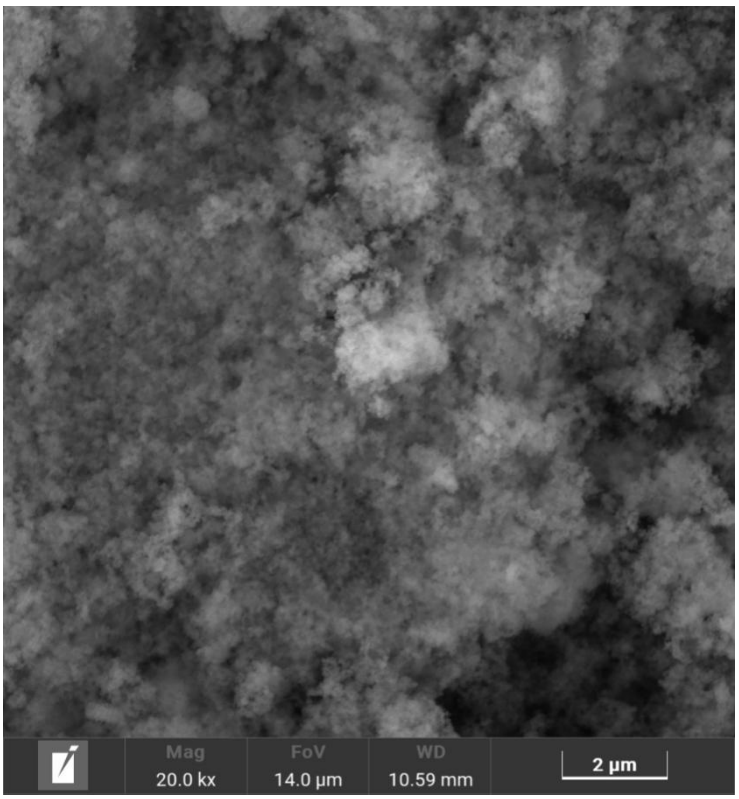

Figure S13. The SEM image of resulting $FePO_4$ particles in the comparative hydrometallurgical process.